

Colloidal crystallization in the quasi-two-dimensional induced by electrolyte gradients

A. Reinmüller, E. C. Oğuz, R. Messina, H. Löwen, H. J. Schöpe et al.

Citation: *J. Chem. Phys.* **136**, 164505 (2012); doi: 10.1063/1.4705393

View online: <http://dx.doi.org/10.1063/1.4705393>

View Table of Contents: <http://jcp.aip.org/resource/1/JCPA6/v136/i16>

Published by the American Institute of Physics.

Additional information on J. Chem. Phys.

Journal Homepage: <http://jcp.aip.org/>

Journal Information: http://jcp.aip.org/about/about_the_journal

Top downloads: http://jcp.aip.org/features/most_downloaded

Information for Authors: <http://jcp.aip.org/authors>

ADVERTISEMENT

The advertisement features the AIP Advances logo with three orange spheres above the word "Advances". Below the logo, the text "Special Topic Section: PHYSICS OF CANCER" is displayed in large, bold, white letters. Underneath that, the question "Why cancer? Why physics?" is shown in white. A blue button at the bottom right contains the text "View Articles Now". The background of the ad has a green and yellow abstract pattern.

Colloidal crystallization in the quasi-two-dimensional induced by electrolyte gradients

A. Reinmüller,¹ E. C. Oğuz,² R. Messina,^{2,3} H. Löwen,² H. J. Schöpe,¹ and T. Palberg¹

¹Institut für Physik, Johannes Gutenberg-Universität Mainz, Staudingerweg 7, 55128 Mainz, Germany

²Institut für Theoretische Physik II, Heinrich-Heine-Universität Düsseldorf, Universitätsstraße 1, 40225 Düsseldorf, Germany

³Laboratoire de Chimie et Physique - Approche Multi-Echelle des Milieux Complexes (LCP - A2MC, EA4632), Université de Lorraine, Institut de Chimie, Physique et Matériaux (ICPM), 1 Bld Arago, 57078 Metz - Cedex 3, France

(Received 8 November 2011; accepted 5 April 2012; published online 26 April 2012)

We investigated driven crystal formation events in thin layers of sedimented colloidal particles under low salt conditions. Using optical microscopy, we observe particles in a thermodynamically stable colloidal fluid to move radially converging towards cation exchange resin fragments acting as seed particles. When the local particle concentration has become sufficiently large, subsequently crystallization occurs. Brownian dynamics simulations of a 2D system of purely repulsive point-like particles exposed to an attractive potential, yield strikingly similar scenarios, and kinetics of accumulation and micro-structure formation. This offers the possibility of flexibly designing and manufacturing thin colloidal crystals at controlled positions and thus to obtain specific micro-structures not accessible by conventional approaches. We further demonstrate that particle motion is correlated with the existence of a gradient in electrolyte concentration due to the release of electrolyte by the seeds. © 2012 American Institute of Physics. [<http://dx.doi.org/10.1063/1.4705393>]

I. INTRODUCTION

Many of the properties of crystalline solids are strongly influenced by the micro-structure of the sample. This micro-structure is controlled during crystallization by a complex interplay of crystal nucleation, growth, and ripening. For bulk situations but also for crystal growth from substrates it is successfully modelled by classical theories and their adaptations to the particular boundary conditions.¹ This behaviour is known well for metals and other atomic substances, but is also observed in colloidal model systems. Their crystallization has intensely been investigated² due to the advantages of space and time resolved measurements and tunability of the interparticle interaction.³ Colloidal melts and crystals are particularly well suited to surpass the restrictions for structure, growth kinetics and morphology present in crystallization from an undercooled melt. Rather, the crystallization scenario is flexibly altered by external influences. External fields,^{4,5} such as electric fields,^{6–8} optical fields,⁹ shear forces,¹⁰ structured templates,¹¹ or specific confining geometries,¹² have been successfully applied to achieve particular micro-structures not available from undisturbed bulk samples.

Experiments were also conducted in confinement to narrow slit geometries. Theoretically, crystallization in strictly 2D systems may proceed via a two step process involving an intermediate hexatic phase rather than by a first order transition involving nucleation and growth.¹³ Experimentally this possibility is still under discussion,⁴ mainly due to the fact that many experimental systems are not strictly 2D. In both situations, 2D and 3D, the main focus so far was on a control of the crystallite size,¹⁴ the competition

between wall-crystal and bulk-crystal formation,¹⁵ or crystal orientation.^{10,16}

We here report preliminary experimental studies combined with Brownian dynamics simulations aiming at a controlled *positioning* of heterogeneously nucleated crystals of predetermined size. We demonstrate experimentally, that positioning of crystals can be achieved by arbitrarily locating seed particles which release micro-ions. The charged colloidal spheres move in reaction to the formed lateral electrolyte concentration gradients and gravity to accumulate at the seeds and there subsequently crystallize. Starting from a thermodynamically stable colloidal fluid, the final crystallite size is determined by the strength and range of the electrolyte gradients. Furthermore, the particular seed size and shape determine whether single-domain or multi-domain crystals emerge. The experiments reported are at present restricted to the study of crystal formation at single seeds of some 10 μm size placed on the lower plate in a narrow slit geometry. Due to gravity and the use of large colloidal particles this results in monolayer colloidal fluids and crystals. Our method of micro-structure control should, however, be applicable also to 3D situations with many seeds and/or meta-stable colloidal shear melts, thus offering the potential to grow large micro-structured polycrystalline solids with arbitrary crystallite patterns. While the underlying microscopic mechanism is not unequivocally identified from the crystallization experiments and subsequent additional investigations, the phenomenology of the crystal formation is well reproducible; as is the confirmation of the observed micro-structures in simulations assuming a convergent solvent flow. In principle, this offers the future possibility to design extended multi-crystal

micro-structures based on given experimental flow direction and strength. The detailed correlation of these flow conditions to the experimental boundary conditions remains an open question at present. We, therefore, also present further experiments motivated by earlier findings on particle motion in electrolyte gradients both in the bulk and close to a substrate.^{17–20}

The remainder of the paper is organized as follows. In the Sec. II A, we first shortly introduce the employed colloidal particles, seed particles and the microscopic techniques in the experimental section. In the Sec. II B, we then explain the analysis of the microscopically observed crystal growth by image processing and analysis techniques and present our results obtained on isolated seed particles. In the Sec. III we shortly present the employed simulation techniques and then highlight our results on flow driven crystallization with respect to dependence of the micro-structure on seed size and shape and the finite final crystallite size. The Sec. IV A compares the obtained results and demonstrates the good qualitative agreement between experimental findings and simulation results. The Sec. IV B presents the additional measures taken to explore the underlying mechanism and discusses their results in the light of previous experimental and theoretical work. It is demonstrated that crystallization is unequivocally linked to the application of electrolyte gradients. The resulting flow conditions, however, seem to be crucially dependent on the background electrolyte concentration and the chosen cell geometry. This discussion part therefore, poses the interesting challenge of clearly discriminating electrophoretic, chemiphoretic, osmotic, and electro-osmotic contributions to flow generation in future experiments and their description in a combined model. Finally a short conclusion is given. The future perspective of crystal patterning is shortly touched. Further theoretical considerations can be found in the Appendix. Further photographic material can be found online in the supplemental materials.

II. EXPERIMENTAL SECTION

A. Experiment

In our experiments, we used suspensions of negatively charged colloidal Polystyrene spheres (diameter $2a = 5.19 \pm 0.08 \mu\text{m}$, Batch No PS/Q-FB1036, Microparticles Berlin GmbH, Germany) in water. The suspension was prepared at a bulk volume fraction $\phi \approx 8\%$ under strongly deionized conditions in a special tube circuit containing a mixed bed ion exchanger column.²¹ Samples were observed in a home-built microscopy cell with parallel plate geometry which was connected to the conditioning circuit. Care was taken to seal the cell interior against contamination with airborne carbon dioxide and the ion concentration was monitored *in situ* using an integrated conductivity measurement cell. The distance between the opposing flat quartz glass windows was adjusted by piezo actuators. During conditioning the slit height was large to allow for fast and efficient homogenization and deionization of the sample. After reducing the ion concentration to significantly less than $1 \mu\text{mol/l}$ the pump was stopped and the horizontal confining cell walls were adjusted to a typical distance of $d \approx 15 \mu\text{m}$ for observations on colloidal

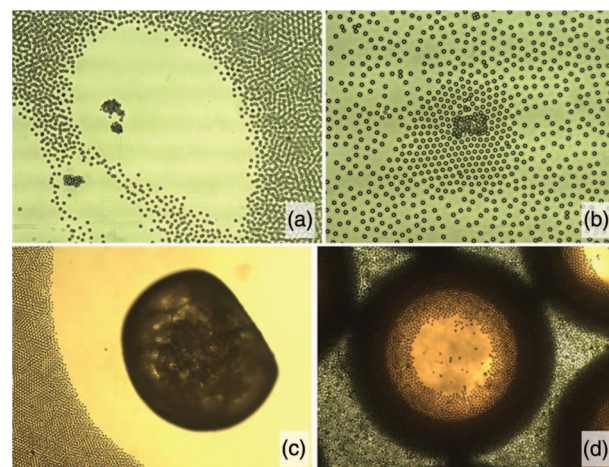


FIG. 1. Voids free of particles in a bilayer system (a), $565 \times 420 \mu\text{m}^2$ and particle accumulation in a monolayer system (b), $360 \times 290 \mu\text{m}^2$ around isolated fragments of ion exchange resins. Similar influences of macroscopic ion exchange resin objects on sedimented colloidal particles were frequently observed: Void formation around anion exchange resin (“A-seed”, (c), $1170 \times 880 \mu\text{m}^2$) and accumulation of mobile particles in the circular gap between a cation exchanger sphere and the quartz substrate (“C-seed”, (d), $720 \times 540 \mu\text{m}^2$).

monolayers crystallizing at small seed particles. The cell was placed on the stage of an inverted optical scientific microscope (DM-IRBE, Leica, Germany) and observed through a $20\times$ objective using a standard video camera. The employed seed particles were small pieces of ion exchange resin (Amberlite K306, Roth GmbH, Germany) which either were already present in the cell after escaping from the ion exchanger column of the circuit or were deliberately added. Their position was directed by the flow conditions during conditioning, but the seeds remained stationary during measurements. For the experiments with large ($700 \mu\text{m}$) seed particles larger cell heights or ion exchange resin seeds placed on a quartz substrate covered by a drop of suspension were employed.

Fluid monolayers settled under gravity formed within less than 1 min after stopping the pump. Strong effective interactions between the small ion exchange resin fragments and the surrounding colloidal particles were observed: In some cases, voids free of particles formed (cf. Fig. 1(a)). In other cases, attraction of particles happened leading to accumulation and even to crystallization (cf. Fig. 1(b)), on which we focus in this paper. Both effects occurred on timescales of about 5 min. Similar particle depletion and accumulation effects were frequently observed also at macroscopic anion (cf. Fig. 1(c)) exchange resin beads (A-seeds) and cation (cf. Fig. 1(d)) exchange resin beads (C-seeds). In particular, for the case of cation exchanger, significant convection-like fluid flow leading to particle accumulation could be traced under suitable experimental geometries.²²

Fig. 2 shows a sequence of optical micrographs of the same crystal growing from a small seed particle at different times with time intervals of each 100 s. The Airy-discs of the particles appear as bright circular dots on a dark background with strongly increased camera contrast in the phase contrast mode. The irregularly shaped seed in the image center consists of an ion exchange resin fragment of greenish

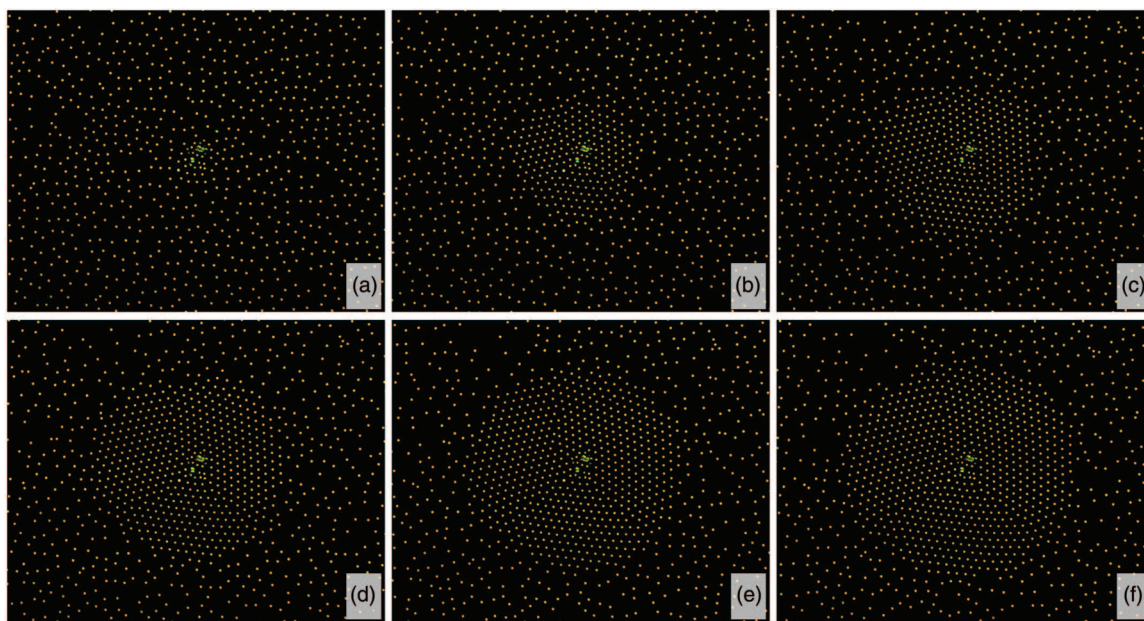


FIG. 2. Growth of a three-domain monolayer crystal on a seed at $t = 0$ s (a), $t = 100$ s (b), $t = 200$ s (c), $t = 300$ s (d), $t = 400$ s (e), and $t = 500$ s (f); field of view: $360 \times 290 \mu\text{m}^2$.

appearance and immobile colloidal particles. In this example, an almost circular monolayer crystal with triangular structure is formed. The three domains grow with a steadily decreasing radial growth velocity. Recording of frames was stopped when there were no significant changes in the system evident any more. Each new incoming particle arranged without a noticeable delay time into the crystal. Thus, the crystal growth velocity was limited by the particle transport. Except for a few particles already attached to the seed all particles stayed mobile. At other seed particles, mono-domain crystals but also crystals with more than one domain were observed. Typical crystal lattice constants were in the range $d_{NN} \sim (8.0 \pm 0.5) \mu\text{m}$, i.e., $d_{NN} \sim 3a$, and small crystal distortions were present. Some of the crystals were noticeably asymmetric, i.e., not perfectly circular (cf. Fig. 1(b)), and not well centered around the seed.

Fig. 3 shows particle trajectories corresponding to Fig. 2 in the time interval beginning at $t = 120$ s and ending at $t = 180$ s. The trajectories display mainly a directed radial motion superimposed by random Brownian motion. A slight asymmetry in the field of trajectories is visible: Particles at the right margin display a more pronounced directed motion than particles at the left margin. This might be due to small local asymmetries in the confining geometry or the released electrolyte gradient or due to weak large-scale drift currents as a result of slow mechanical relaxation processes of the setup components. Significant initial fluid flow resulting from positioning the confining walls ceased within 1 min.

Experimental observations were qualitatively well reproducible after homogenizing the suspension again by pumping or by fast vertical movements of the piezo actuators. Both induce strong solvent currents which shear melt existing crystalline structures. Without external disturbance crystals were stable as long as the experimental conditions were stable. However, the lattice constant shrank by some 10% over about

1 h due to contamination with salt ions screening the interparticle repulsion.

B. Analysis of crystal growth

For quantitative analysis of the crystallization process first a standard tracking algorithm²³ was applied on the image sequences. Using the gathered particle positions the six-fold bond order parameter

$$p_6 = \sqrt{\psi_6^* \psi_6} \geq 0.9 \quad (1)$$

with $\psi_6 = \frac{1}{6} \sum_{j=1}^6 e^{6i\theta_j}$ and θ_j denoting the angle between a nearest neighbor bond and a fixed reference axis and the

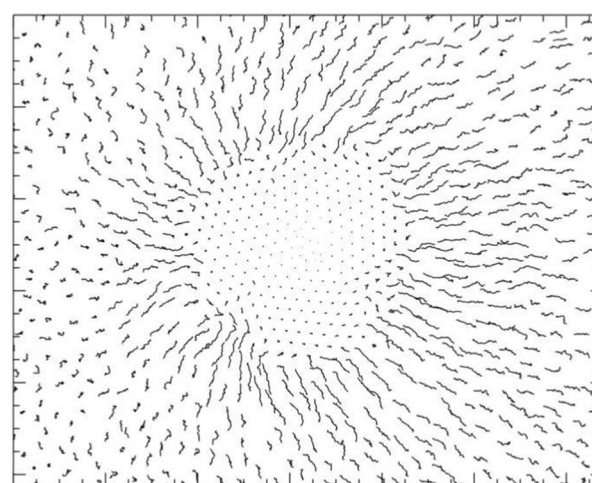


FIG. 3. Particle trajectories of the same sequence from Fig. 2 between $t = 120$ s and $t = 180$ s. Initially a fast ceasing fluid flow was running from right to left as a result of positioning the confining walls.

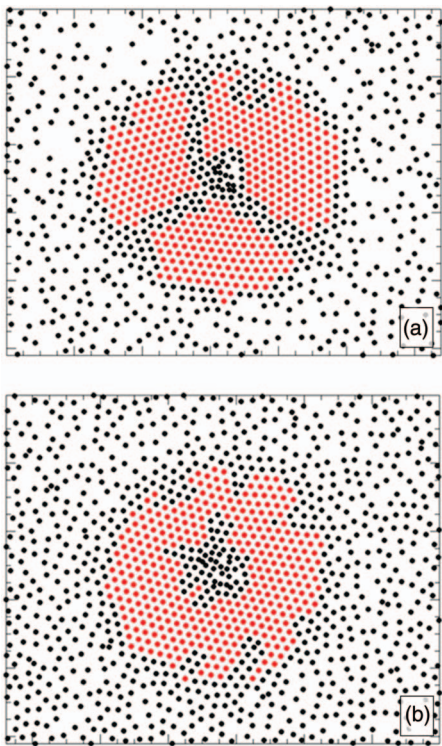


FIG. 4. Analysis of the experimentally observed three-domain crystal (a), cf. Fig. 2 and mono-domain crystal (b) each at $t = 500$ s; crystalline particles fulfilling the local criteria according to Eqs. (1) and (2) are drawn in red, all others in black. A few doublets of coagulated particles lead to local defects in the crystal. ($360 \times 290 \mu\text{m}^2$).

relative bond length deviation

$$b_6 = \frac{1}{6} \sum_{j=1}^6 \frac{|l_j - \bar{l}|}{\bar{l}} \leq 0.1 \quad (2)$$

with \bar{l} denoting the average bond length between a particle and its six nearest neighbors were used for identifying crystalline particles.²⁴ Both p_6 and b_6 were calculated for each particle individually. Fig. 4 shows the final state of two growth sequences each after 500 s. Crystalline particles with respect to formulae (1) and (2) are plotted in red, all others in black. The poly-domain structure in Fig. 4(a) and the mono-domain structure in Fig. 4(b) are clearly visible. Further, from image analysis, also the average nearest neighbor distance of crystalline particles of $d_{NN} = (7.6 \pm 0.3) \mu\text{m}$ in both cases was obtained.

The corresponding crystal sizes in terms of crystalline particle numbers $N_c(t)$ and the effective crystal radii

$$R_c(t) = \sqrt{N_c(t)/\pi\rho_c} \quad (3)$$

as a function of time are shown in Figs. 5(a) and 5(b), respectively. Here ρ_c denotes the area particle number density of the crystal calculated out of the average nearest neighbor distance d_{NN} , that both did not change significantly during growth.

Flattening of the curves indicate an exponentially decreasing growth velocity, which is explained in detail with a theoretical model in the Appendix:

$$R_c(t) = R_\infty - \bar{R}e^{-\lambda t}, \quad (4)$$

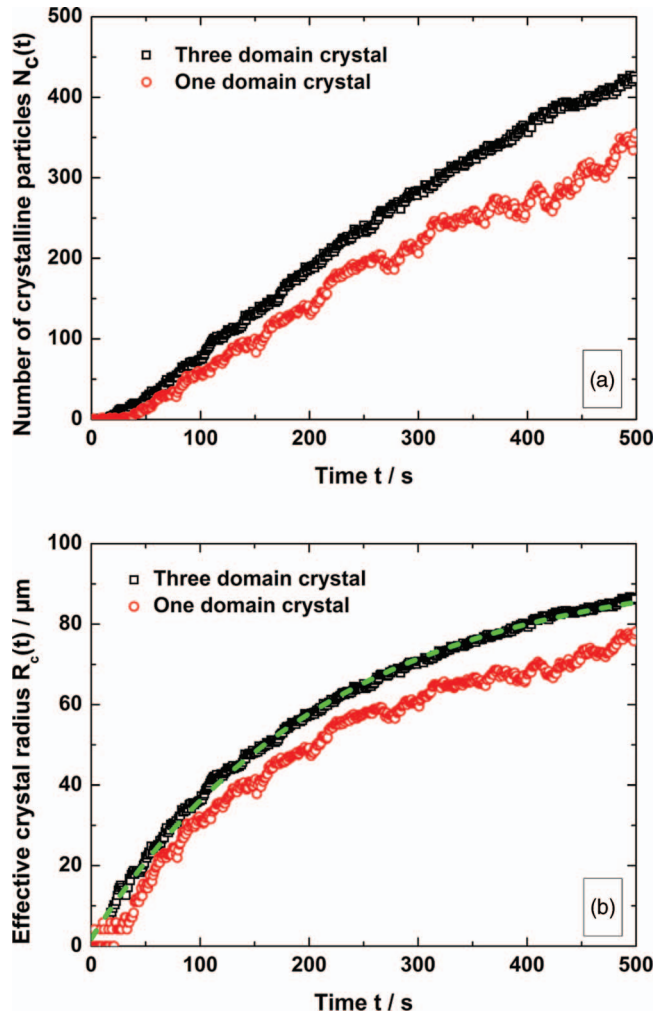


FIG. 5. Experimentally observed crystal growth: Number of crystalline particles $N_c(t)$ (a) and effective crystal radius $R_c(t)$ (b) vs. time t ; black curves correspond to the three-domain crystal (Fig. 4(a)) and red curves correspond to the mono-domain crystal (Fig. 4(b)). The green dashed line in (b) is an exponentially saturating fit to the black curve.

where \bar{R} is a fit parameter and λ the characteristic rate constant. R_∞ denotes the saturation radius, which is expected to set in for large times. An according fit function is drawn in green in Fig. 5(b).

For the crystallization events presented here the saturation radii amount to $R_\infty \approx 95 \mu\text{m}$ (three-domain crystal) and $R_\infty \approx 80 \mu\text{m}$ (mono-domain crystal), and the characteristic time constants amount to $\lambda^{-1} \approx 215 \text{ s}$ and $\lambda^{-1} \approx 200 \text{ s}$, respectively. Those values may later serve for comparison with results of the theoretical modeling of the system.

III. SIMULATIONS

We performed Brownian dynamics simulations of purely repulsive point-like particles in two dimensions. We assume the particles to be confined in a disk and interact via a Yukawa pair potential²⁵

$$V(s) = V_0 \frac{e^{-\kappa s}}{\kappa s} \quad (5)$$

with s denoting the interparticle separation and κ the inverse screening length. The strength of the potential energy is thereby set by the amplitude V_0 . Motivated by the experimentally observed convection-like currents²² leading to particle accumulation at large cation exchanger seeds, we model the effective attractive trap force in 2D by a stationary radial flow field of the form:

$$\mathbf{F}_0(\mathbf{r}) = \gamma \mathbf{u}(\mathbf{r}) = -\gamma \frac{A}{r^3} \mathbf{r}, \quad (6)$$

where γ is the Stokesian friction coefficient, \mathbf{u} the flow velocity at \mathbf{r} (relative to the origin with $r = |\mathbf{r}|$), and A a positive flow amplitude. Herein, we physically assume that the convective flow is sufficiently weak that accumulated particles stay confined to the monolayer due to gravity. The inverse square distance dependency of the flow is justified by the incompressibility of the fluid $\nabla \cdot \mathbf{u}(\mathbf{r}) = 0$ in three dimensions. The equation for the trajectory $\mathbf{r}_i(t)$ of colloidal particle i obeying Brownian motion (neglecting hydrodynamic interactions) after a finite time step δt reads:

$$\mathbf{r}_i(t + \delta t) = \mathbf{r}_i(t) + \frac{D_0}{k_B T} \mathbf{F}_i(t) \delta t + \mathbf{u}(\mathbf{r}_i) \delta t + \delta \mathbf{W}_i, \quad (7)$$

where $D_0 = k_B T / \gamma$ denotes the free diffusion constant, $k_B T$ the thermal energy, and $\mathbf{F}_i(t)$ is the total conservative force acting on particle i stemming from the pair interactions (i.e., $V(s)$) and a repulsive particle-wall interaction due to an outer circular boundary. The latter is chosen to be a truncated and shifted 6–12 Lennard-Jones potential confining the particles within a disk of a large radius $R = 900/\kappa$. The third term on the right hand side of Eq. (7) is merely due to the flow field, see Eq. (6). Finally, the random displacement $\delta \mathbf{W}_i$ is sampled from a Gaussian distribution with zero mean and variance $2D_0\delta t$ (for each Cartesian component) fixed by the fluctuation-dissipation relation.

In the simulations, the system consists of $N = 5000$ particles with an initial overall fluid density $\rho_0/\kappa^2 \approx 0.002$. We achieved good qualitative agreement with the experimental findings for a flow amplitude of $A\kappa/D_0 = 10^4$ and an interaction strength $V_0/k_B T = 5 \times 10^7$. The time step is chosen as $\delta t = 3 \times 10^{-5}\tau$, where $\tau = 1/(\kappa^2 D_0)$. The crystal formation process strongly depends on the shape of the seed. Seeds were realized by placing an arbitrarily shaped area of suitable extension in the disk centre which acted for the particles as hard core repulsive area. The particles in the first layer are thus still mobile and may adjust their spacing according to their mutual interaction. Upon inspecting the experimental data (cf. Fig. 4), we have considered different typical shapes of impenetrable seeds. Thereby, differently shaped poly-crystals grow depending on the seed shape. Representative snapshots can be found in Fig. 6 for two different shapes of the seed. About the kite-like shaped seed in Fig. 6(a) we obtained a three-domain crystal with three grain boundaries. We further show a second example of a circular seed yielding a mono-domain crystal with one grain boundary (cf. Fig. 6(b)).

The three-domain crystal as well as the mono-domain crystal ceased to grow at $\kappa R_\infty \approx 340$. The three-domain crystal density accounts to $\rho_c/\kappa^2 \approx 0.0027$ at saturation, whereas the density of the mono-domain crystal is $\rho_c/\kappa^2 \approx 0.003$. The

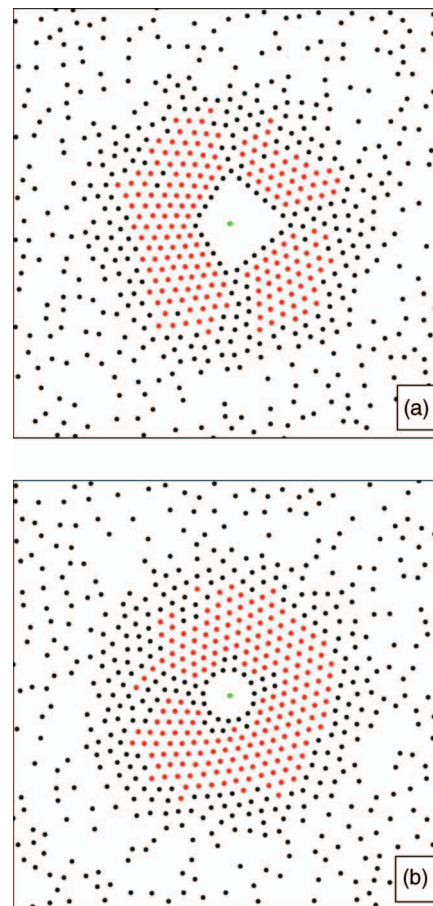


FIG. 6. Simulation snapshots of a three-domain (a) and a mono-domain crystal (b) each at $t = 500\tau$. The green dots in both illustrations indicate the origin of the system. The particle flow into the polygonal (a) and spherical (b) area is prohibited. Analogue to Fig. 4, the red particles are crystalline, the black ones not. Field of view: $250 \times 250/\kappa^2$.

number of crystalline particles $N_c(t)$ and the crystal radii $R_c(t)$ from the simulation data are plotted in Fig. 7, from which we extract the characteristic decay time of the exponentially saturating crystal growth by fitting $R_c(t)$, see Fig. 7(b). In the considered time interval ($0 < t/\tau < 500$) the characteristic time has been determined to be $\lambda\tau \approx 5 \times 10^{-3}$.

IV. DISCUSSION

A. Crystal growth

Our simulations agree qualitatively well with our experimental observations. The main equivalences are the formation of triangular monolayer crystals, the evolution of different micro-structures on different seeds as well as the exponentially saturating crystal growth. In addition, they also clearly show that crystallization follows accumulation by the imposed flow.

The occurrence of only triangular crystal symmetry in both experiments and simulations is in agreement with a long-range attraction that enforces an efficient packing with respect to potential energy due to the short range particle interactions. In many cases, there are slight lattice distortions visible that might be correlated with the local attractive force, but on the

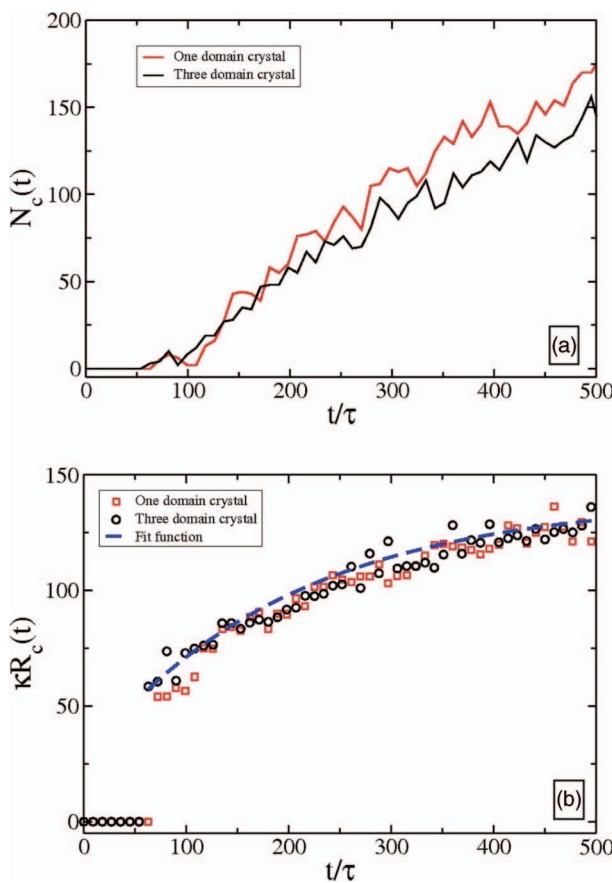


FIG. 7. Simulated crystalline particle number $N_c(t)$ (a) and effective crystal radii $\kappa R_c(t)$ (b) of the three-domain (black curve/circles) and the mono-domain (red curve/squares) crystals of Figs. 6(a) and 6(b) vs. the reduced time t/τ . The blue dashed curve in (b) corresponds to an exponentially saturating fit curve with characteristic decay time $\lambda\tau \approx 5 \times 10^{-3}$.

other hand, those also might occur to reduce stress at domain boundaries. Significant radial variations of the lattice constant were not resolved.

Our observations indicate that no nucleation barrier is present in both simulation and experiment. Therefore, the number of domains formed depends neither on thermodynamics nor on nucleation kinetics. Rather, the micro-structure crucially depends on the seed geometry. Hence, we payed particular attention to this point in a large number of simulation runs. Point-like seeds geometrically allow perfect single-domain crystals that actually occurred in simulations. Seeds incommensurate with a triangular symmetry-like squares or irregular forms-induced poly-domain structures (cf. Fig. 6(a)) in the simulations. By contrast, the experimental seed geometries were rather irregular and not well specified. Therefore, so far no reliable relation between seed geometry and resulting morphology can be obtained experimentally. Seed materials providing the opportunity of specifically being shaped as an alternative to brittle ion exchange resins would here be of great advantage.

Further, the exponentially saturating crystal growth is evident in experiments as well as in simulations, where also saturation sets in for large times (cf. Figs. 5(b) and 7(b)). As theoretically clearly shown (see the Appendix) this behavior is also the result of a competition between the attractive,

time independent, radially decaying force field, and the interparticle repulsion by already crystalline particles. The evaluated saturation radii R_∞ of both experiments and simulations might be biased if too small particle numbers in the system are used. In this case crystallization stops when no further incoming particles are available. This effect does obviously not influence our experimental observations since the area particle number densities of the surrounding fluid ($\rho_f \approx 0.007/\mu\text{m}^2$ and $\rho_f \approx 0.009/\mu\text{m}^2$ for the three- and the mono-domain crystal, respectively) do not change significantly during the crystallization processes. In our simulations, this artifact was avoided by using particle numbers significantly larger than that of the saturated crystal.

A quantitative comparison, however, is difficult since two important experimental parameters, namely, the experimental inverse screening length κ and the interaction amplitude V_0 in the narrow slit between the charged substrates, are principally unknown due to presence of substrate counter ions as well as salt ions set free by the seed. Further, the particle diffusion coefficient D_0 in the surface plane of the substrate is difficult to estimate due to hydrodynamic particle-wall interactions as well as particle-particle interactions. Still, good qualitative agreement was obtained using physically sensible estimates of these values. Using the bulk values $\kappa = (2.7 \pm 0.7)/\mu\text{m}$ obtained from conductivity measurements and $D_{0,Bulk} = 0.085 \mu\text{m}^2/\text{s}$ obtained from the Stokes-Einstein relation together with the experimental values λ and R_∞ extracted from the image sequences, we get $\lambda\tau = (7.5 \pm 2.8) \times 10^{-3}$ and $\kappa R_\infty = (260 \pm 70)$ for the three-domain crystal and $\lambda\tau = (8.1 \pm 3.0) \times 10^{-3}$ and $\kappa R_\infty = (220 \pm 60)$ for the mono-domain crystal. Despite the fact that these experimental values do not perfectly match the simulated values $\lambda\tau \approx 5 \times 10^{-3}$ and $\kappa R_\infty \approx 340$, their orders of magnitude are equal.

Although the particle motion happens in quasi-2D, the attractive force field (cf. Eq. (6)) was modelled assuming a velocity field $|\mathbf{u}(\mathbf{r})| \propto 1/r^2$ rather than a field $|\mathbf{u}(\mathbf{r})| \propto 1/r$. This is justified since a convection-like solvent flow field will also under the given experimental conditions have vertical velocity components. For comparison also simulations using velocity fields $|\mathbf{u}(\mathbf{r})| \propto 1/r$ were performed. These lead to similar accumulation and crystallisation scenarios, which, however, matched the experimental observations less quantitatively. Extremely long-ranged attractions compared to typical interparticle distances occurred. In summary, it can be said that here reasonably good qualitative agreement between experiments and simulations is achieved by using an effective, pure 2D, long-ranged attractive potential for the theoretical description instead of an explicit hydrodynamic model.

B. Gradient-induced particle transport

The crystallization experiments can be well reproduced using certain experimental boundary conditions, and, furthermore, the experiments can be qualitatively well modelled by referring only to the flow field. The details of the underlying mechanism are, however, still not fully understood. Their explicit discrimination and theoretical treatment is beyond the

scope of the present paper and would require monitoring of micro-ion currents and solvent flow. As this question, nevertheless, is extremely relevant for applications, we here give a preliminary collection of possibilities for particle transport. Based on additional experiments we can exclude several of these and suggest an ion gradient-induced particle transport as explanation of our observations.

Particle transport may, in principle, be caused by a direct seed-particle interaction, by a seed-induced gradient of some kind or by solvent flow. As in all our experiments with C-seeds, we observe an accumulation of colloidal particles in the sedimented layer(s), while at A-seeds, we regularly observed void formation, we may safely exclude thermal convection due to seed heating under illumination. This mechanism would change the amplitude of convective flow in dependence on seed material, but not its sign. Further, we observed the accumulation also under conditions of very low initial particle concentration.²² Particles as far away from the seed as a hundred microns were attracted or repelled immediately after stopping the mixing flow. By this observation, we can exclude a direct electrostatic attraction or repulsion, which is strongly screened over these distances even at very low particle and salt concentration ($\kappa^{-1} \leq 1 \mu\text{m}$). In addition, we also may exclude gradients in particle-particle interaction. Particles far away from the C-seed are non-interacting under these conditions. Accumulated particles are interacting with a strong repulsion. Therefore, the direct particle-particle interaction would tend to push the accumulated particles outward. This argument also holds for the A-seeds, where the osmotic pressure in the bulk will tend to refill any void.

In all our experiments at large cell heights or without upper confining wall we observed the formation of annular currents.²² In particular, directly above large C-seeds we observed colloidal particles with a pronounced upward particle motion. For large seeds the currents often were too fast to allow for crystallization. As a general trend, the convection diminished with decreasing seed size. For cell heights below 30 μm (limiting the seed size to less than 30 μm) convection was not demonstrable, as the presumably present current became too weak, to lift our large colloidal particles from their monolayer. A demonstration would be possible with much smaller particles not subject to gravitational settling. These would become traceable using image correlation velocimetry,²⁶ which is currently under development in our group.

Recently, Ibele *et al.*²⁰ reported similar particle depletion and/or accumulation effects, although without order formation. Using different chemicals in detail, they especially have observed the formation of both “schools” and voids of colloidal tracer particles around seeds on a substrate. Based on analytical calculations by Anderson and Prieve^{17–19} they identify as physical origin different concentration profiles of positive and negative ions released by the seeds.

To test the presence of ion concentration gradients we used pH-indicator liquids together with isolated pieces of resins. Significant characteristic color changes close to the resins were observed after minutes (cf. Fig. 8). Both types of resin (Amberlite K306, Roth GmbH, Germany) release large

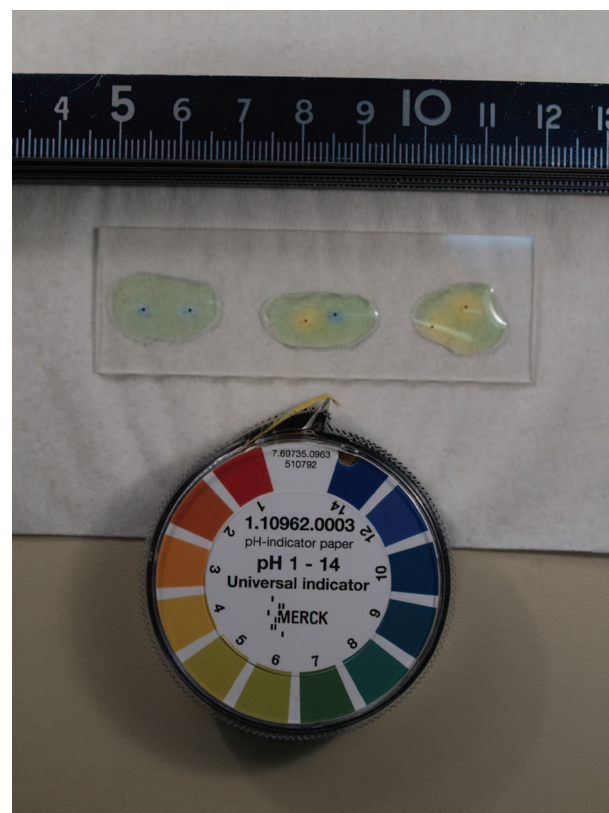


FIG. 8. Color change of pH-indicator liquid close to isolated pieces of ion exchange resin on a glass microscopy slide: Acidic color change at cation exchange resins (yellow, pH ≈ 4) and basic color change at anion exchange resins (blue, pH ≥ 8) occurred within 5 min.

amounts of their activator electrolytes. Those are hydrochloric acid (HCl) and sodium hydroxide (NaOH) for C-seeds and A-seeds, respectively. According to the observed color changes we find a change of electrolyte concentration of about 2–3 orders of magnitude over distances of a few mm.

According to Anderson *et al.*,^{17–19} a gradient of electrolyte concentration is inevitably coupled to the existence of local electric fields. This is due to the different micro-ionic diffusivities creating a space charge region of extension $O(\kappa)$, with the faster micro-ion drifting ahead and determining the field direction. The field strength is determined by the diffusivity difference and the local average concentration. Charged colloidal particles will react both to the gradient itself (drifting upward due to the entropy of mixing) and the field. Their electrophoretic reaction to the field depends on their charge sign and the field direction. In the case of HCl released by a C-seed, H^+ has a significantly larger bulk diffusion coefficient than Cl^- ($D(\text{H}^+) = 9.3 \times 10^{-5} \text{ cm}^2/\text{s}$ and $D(\text{Cl}^-) = 2.0 \times 10^{-5} \text{ cm}^2/\text{s}$ at infinite dilution at 25 °C). Negatively charged particles in such a gradient, where the proton is ahead and the field is directed towards the large concentration region, will show an electrophoretic drift against the gradient. Both effects superimpose and the resulting so-called *diffusiophoretic* drift velocity and direction can be estimated analytically for $\kappa a > 1$ or have to be calculated numerically for smaller values of κa .^{17,18}

The local fields will further interact with the electrical double layer (EDL) of the cell walls.²⁰ Again two points have

to be considered. First, the imposed electrolyte gradient superimposes with the concentration profile of the wall-EDL. A lateral difference in osmotic pressure within the EDL results. This will induce an osmotic flow of solvent volume elements of the EDL directed along the wall towards smaller electrolyte concentrations. Second, for a negatively charged wall, the EDL contains dominantly cationic species. Volume elements of the solvent within the EDL hence carry a space charge and will be accelerated by the local, gradient-induced field. Similarly to the electro-osmotic effect of solvent flow along a charged wall under the influence of an *externally* applied field, this reaction of the solvent to the local gradient-induced fields results in a macroscopic flow along the cell wall. For the example of a C-seed lying on the quartz wall, the direction of the electro-osmotic flow is towards the seed. Both osmotic and electro-osmotic effects superimpose. Due to the incompressibility of the solvent an annular convection pattern has to evolve either with the formation of a centrosymmetric depletion zone or with an upward flow in the centre of the convergent flow. For the case of an A-seed osmotic and electro-osmotic effects will drive the solvent outward. For a C-seed both effects compete. According to our experimental observations, however, we find that the electro-osmotic term dominates at least for large C-seeds. The flow induced by C-seed released gradients²² or other kinds of gradients²⁰ may even become strong and fast enough to prevent order formation.

Combining our experimental observations with the theoretical considerations we unequivocally identify the presence of an electrolyte gradient to be the cause of the particle transport. The involved mechanism for large C-seeds is convective and thus dominated by the convergent electro-osmotic solvent flow. Crystallization is possible, once the local particle number density exceeds the salt concentration dependent freezing density and the local shear forces are small enough. We qualitatively sketch the field generating electrolyte gradients around a cation exchange resin particle in Fig. 9(a). Fig. 9(b) exemplarily shows the resulting laterally converging, electro-osmotically-induced fluid flow for the case of a large C-seed. Due to mass conservation the geometry of this flow field enforces an upwards directed vertical flow in the convergence region, i.e., at the seed position. For suitable combinations of particle mass density and current strength, the sedimented colloidal particles are dragged along towards the resin fragment, but cannot follow the upward flow due to the presence of gravity.

For smaller seeds the cause of particle transport is also given by the presence of an electrolyte gradient. The involved mechanisms could, however, not be discriminated from the present experiments. We anticipate that a dominance of electro-osmotic currents is still present, but, in particular for an additional upper wall present and small cell heights also significantly altered flow patterns or even a suppression of convective flow could in principle occur. In that case the other mechanisms would gain importance. In principle, an attraction may even occur for the case of a small A-seed, when the inward diffusiophoretic particle motion exceeds an outward electro-osmotic solvent flow. Fortunately, for the qualitative comparison between experimental observations and simula-

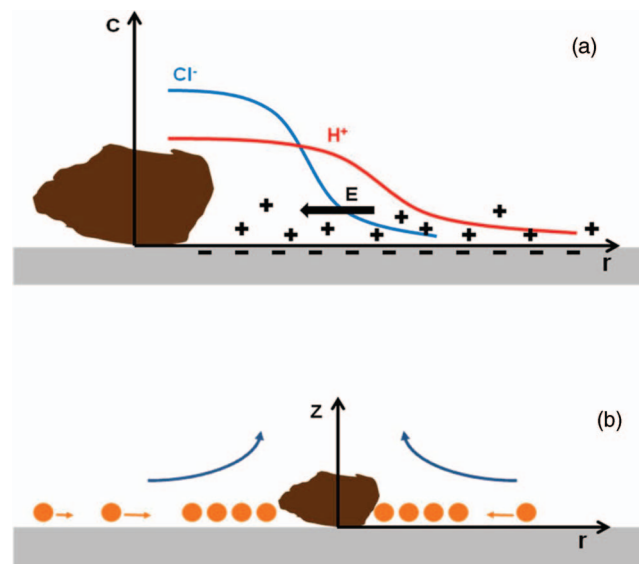


FIG. 9. Qualitative sketch of the electro-osmotic mechanism: (a) Spatial profiles of H^+ and Cl^- ion concentrations c (red and blue curve, respectively) vs. distance r from a C-seed (brown) releasing HCl ; a balancing electric field E arises that drives the mobile counter ions (plus-signs) within the diffuse part of the electrical double-layer of the substrate (grey bar; immobile substrate surface charges are indicated by minus-signs). (b) Sketch of the electro-osmotically driven flow (blue arrows) inducing accumulation of colloidal particles (orange) next to the seed (brown).

tions using an attractive potential the details of the actual mechanisms do not play a crucial role. Rather, we have shown that whenever there is some kind of particle accumulation enhancing the local particle concentration beyond the threshold density, crystallization occurs.

V. CONCLUSION

In this paper we investigated driven colloidal crystallization by complementary experimental and theoretical approaches. Quasi-2D transport, accumulation, and crystal structure formation in a colloidal monolayer were experimentally induced using locally applied ion concentration gradient fields around cation exchange resin seed objects in slit confinement. Qualitatively equivalent results were obtained by Brownian dynamics simulations using a long-ranged trapping potential in 2D and competitive interparticle repulsion. While we have presented strong evidence for a dominance of electro-osmotic currents in the case of large seeds, the detailed weighting of the different particle transport mechanisms possibly involved remains to be clarified in future experiments. For each given experimental boundary condition we actually expect a complex scenario which poses a number of interesting questions to theory and engineering. Electrolyte gradient-induced mechanisms may also be considered as a possible explanation for anomalous colloidal high density crystals and void structures reported previously.²⁹

The observed driven crystallization process has, to our knowledge, not been described in detail before. The pioneering work of Hachisu,²⁷ who reported the very existence of crystals grown at ion exchange resin beads has, in fact, not been followed by further investigations to observe the crystal

formation kinetics. Nor have there been attempts to study the involved transport mechanisms. Similar observations of crystal formation at sedimented ion exchange resin beads rather have occasionally been mistaken as equilibrium phenomena.²⁸ Hence, our observations are innovative and may provide a novel, flexible method for designing and manipulating spatial distribution and morphology of thin colloidal crystals in fluid dispersion media. Conventional homogeneous and heterogeneous bulk crystallization provide no control of crystallite position and morphology, and fabrication of patterned substrates to induce a particular wall crystal growth pattern is (at least) tedious. Efficient modeling together with the experimental feasibility of flexibly manufacturing seeds, however, would provide the opportunity of designing specific crystalline material. It is conceivable that a printing process can be used to flexibly fabricate substrates, e.g., by soft lithography or just by jet printing. Therefore, it will be necessary to fabricate appropriate seed materials, e.g., a polymeric or gelling matrix that can flexibly be imprinted onto a substrate, where it releases appropriate ionic solutes slowly, and possibly even under external control. The simulations presented above on the other side reproduced the experimental findings for the given boundary conditions remarkably well. This shows in principle, that they will become very useful in designing appropriate seed distributions enforcing desired crystal micro-structures. Apart from industrial relevance for the fabrication of textured iridescent coatings or photonic materials in general, we further anticipate possible uses of such combined approaches for fundamental studies, e.g., to obtain monodisperse grain sizes in polycrystalline materials or well defined multiple grain boundaries.

ACKNOWLEDGMENTS

We gratefully acknowledge financial support by Deutsche Forschungsgemeinschaft (SFB-TR6 projects B1 and D1, Pa459/15-17, Scho1054/3) and technical support by Aditya Kalia, Meerut, India.

APPENDIX: THEORY OF CRYSTAL GROWTH BEHAVIOR

Here, we furthermore develop a simple theory to characterize the crystal growth behavior. We model the system with a coarse-grained one-particle density fluid $\rho(r, t)$ around the origin of the trap where the initial condition $\rho(r, t = 0) = \rho_f$ is imposed. Due to the external trap force we assume a crystallite of radius $R_c(t)$ to be formed at a density $\rho_c > \rho_f$ around the origin. According to the repulsive interparticle force and the decay of the trap force with distance, the growth is supposed to stop after a while. The size of the crystallite can be predicted by applying the continuity equation at the boundary of the crystallite. We here consider the crystallite as a hemisphere (3d) located at the seed. For the number of crystalline particles in the crystallite, $N_c(t)$, we have

$$\dot{N}_c = \rho_c \frac{d}{dt} \left(\frac{2}{3} \pi R_c^3(t) \right) = 2\pi \rho_c R_c^2(t) \dot{R}_c(t). \quad (\text{A1})$$

On the other hand, this must be balanced by the flux of incoming particles, $j(R_c(t)) = \rho_f \frac{F(R_c(t))}{\gamma}$, leading to

$$\dot{N}_c = -2\pi R_c^2(t) \rho_f \frac{F(R_c(t))}{\gamma}, \quad (\text{A2})$$

where $F(r)$ is the total force acting on the particles

$$F(r) = F_0(r) + F_1(r), \quad (\text{A3})$$

which stems from (i) the attractive force from the external trap ($F_0 = |\mathbf{F}_0|$, cf. Eq. (6)) and (ii) the repulsive force from the inner crystallite particles F_1 . The latter can be approximated in the mean-field theory leading to a distance independent force. Detailed calculations with a cutoff $a = \rho_f^{-1/3}$ in the interaction range lead to

$$F_1 = \pi V_0(\rho_c - \rho_f) \frac{1}{2\kappa^2} e^{-\kappa a} (2 + \kappa a), \quad (\text{A4})$$

Equating Eqs. (A1) and (A2) yields

$$\dot{R}_c = \frac{\rho_f}{\rho_c} \left(\frac{A}{R_c^2(t)} - \frac{F_1}{\gamma} \right). \quad (\text{A5})$$

For $t \rightarrow \infty$, R_c will approach its equilibrium (static) value

$$R_\infty = R_c(t \rightarrow \infty) = \left(\frac{A\gamma}{F_1} \right)^{1/2}. \quad (\text{A6})$$

For large time, Eq. (A5) can be linearized to yield

$$\frac{d}{dt} (R_\infty - R_c(t)) = (R_\infty - R_c(t)) \frac{2A\rho_f}{R_\infty^3 \rho_c} \quad (\text{A7})$$

with the solution

$$R_\infty - R_c(t) = \bar{R} e^{-\lambda t}, \quad (\text{A8})$$

where \bar{R} denotes a fit parameter and $\tau = 1/\lambda = R_\infty^3 \rho_c / 2A\rho_f$ the associated decay time. Eq. (A8) implies that the approach towards R_∞ is exponential in time as found in the experiment and simulation, see Figs. 5(b) and 7(b). The saturation radius has been calculated with Eq. (A6) to $\kappa R_\infty \approx 330$ that shows a good agreement between the theory and simulation, too.

¹D. Kashchiev, *Nucleation* (Butterworth-Heinemann, Oxford, 2000); A. N. Kolmogorov, Izv. Akad. Nauk SSSR, Ser. Mat. **1**, 355 (1937); W. A. Johnson and R. F. Mehl, Trans. Am. Inst. Min., Metall. Pet. Eng. **135**, 416 (1939); M. Avrami, J. Chem. Phys. **7**, 1103 (1939); **8**, 212 (1940); **9**, 177 (1941); C. D. van Siclen, Phys. Rev. B **54**, 11845 (1996).

²V. J. Anderson and H. N. W. Lekkerkerker, Nature (London) **416**, 811 (2002); J. L. Harland and W. van Megen, Phys. Rev. E **55**, 3054 (1997); T. Palberg, J. Phys.: Condens. Matter **11**, R323 (1999); K. F. Kelton and A. L. Greer, *Nucleation in Condensed Matter: Applications in Materials and Biology*, Pergamon Materials Series (Pergamon, Elsevier, 2010).

³A. Yethiraj, Soft Matter **3**, 1099 (2007).

⁴U. Gasser, J. Phys.: Condens. Matter **21**, 203101 (2009).

⁵M. Sullivan, K. Zhao, C. Harrison, R. H. Austin, M. Megens, A. Hollingsworth, W. B. Russel, Z. Cheng, T. Mason, and P. M. Chaikin, J. Phys.: Condens. Matter **15**, S11 (2003); H. Löwen, *ibid.* **13**, R415 (2001); **20**, 404201 (2008); A. van Blaaderen, MRS Bull. **29**, 85 (2004).

⁶H. J. Schöpe, J. Phys.: Condens. Matter **15**, L533 (2003); T. Gong, D. T. Wu, and D. W. M. Marr, Langmuir **19**, 5967 (2003).

⁷Y. Solomentsev, M. Böhmer, and J. L. Anderson, Langmuir **13**, 6058 (1997).

⁸M. Böhmer, Langmuir **12**, 5747 (1996).

⁹T. Gong and D. W. M. Marr, Appl. Phys. Lett. **85**, 3760 (2004); J. P. Hoogenboom, D. L. J. Vossen, C. Faivre-Moskalenko, M. Dogterom, and A. van Blaaderen, Appl. Phys. Lett. **80**, 4828 (2002).

- ¹⁰A. Stipp, R. Biehl, T. Preis, J. Liu, A. B. Fontecha, H. J. Schöpe, and T. Palberg, *J. Phys.: Condens. Matter* **16**, S3885 (2004).
- ¹¹Y. Tang, R. M. Malzenbender, R. C. Mockler, W. J. O'Sullivan, and J. A. Beall, *J. Phys. A* **20**, L189 (1987); J. P. Hoogenboom, A. K. van Langen-Suurling, J. Romijn, and A. van Blaaderen, *Phys. Rev. E* **69**, 051602 (2004).
- ¹²H. Löwen, A. Härtel, A. Barreira-Fontecha, H. J. Schöpe, E. Allahyarov, and T. Palberg, *J. Phys.: Condens. Matter* **20**, 404221 (2008); A. B. Fontecha, H. J. Schöpe, H. König, T. Palberg, R. Messina, and H. Löwen, *ibid.* **17**, S2779 (2005).
- ¹³J. M. Kosterlitz and D. J. Thouless, *J. Phys. C* **6**, 1181 (1973); D. R. Nelson and B. I. Halperin, *Phys. Rev. B* **19**, 2457 (1979); A. P. Young, *ibid.* **19**, 1855 (1979).
- ¹⁴T. Palberg, W. Mönch, J. Schwarz, and P. Leiderer, *J. Chem. Phys.* **102**, 5082 (1995).
- ¹⁵M. Franke, A. Lederer, and H. J. Schöpe, *Soft Matter* **7**, 11267 (2011); A. Engelbrecht, R. Meneses, and H. Schöpe, *ibid.* **7**, 5685 (2011).
- ¹⁶B. J. Ackerson and N. A. Clark, *Physica A* **118**, 221 (1983).
- ¹⁷J. L. Anderson and D. C. Prieve, *Sep. Purif. Methods* **13**, 67 (1984).
- ¹⁸D. C. Prieve, J. L. Anderson, J. P. Ebel, and M. E. Lowell, *J. Fluid Mech.* **148**, 247 (1984).
- ¹⁹J. L. Anderson, *Annu. Rev. Fluid Mech.* **21**, 61 (1989).
- ²⁰M. Ibele, T. E. Mallouk, and A. Sen, *Angew. Chem., Int. Ed.* **48**, 3308 (2009).
- ²¹P. Wette, H. J. Schöpe, R. Biehl, and T. Palberg, *J. Chem. Phys.* **114**, 7556 (2001).
- ²²See supplementary material at <http://dx.doi.org/10.1063/1.4705393> for Movies I-VII and Figures I and II.
- ²³J. C. Crocker and D. G. Grier, *J. Colloid Interface Sci.* **179**, 298 (1996).
- ²⁴L. Assoud, F. Ebert, P. Keim, R. Messina, G. Maret, and H. Löwen, *Phys. Rev. Lett.* **102**, 238301 (2009).
- ²⁵H. Löwen, *J. Phys.: Condens. Matter* **4**, 10105 (1992); E. Chang and D. Hone, *Europhys. Lett.* **5**, 635 (1988).
- ²⁶E. J. Stamhuis, *Aquat. Ecol.* **40**, 463 (2006); R. D. Keane and R. J. Adrian, *Appl. Sci. Res.* **49**, 191 (1992).
- ²⁷A. Kose, M. Ozaki, K. Takano, Y. Kobayashi, and S. Hachisu, *J. Colloid Interface Sci.* **44**, 330 (1973).
- ²⁸B. V. R. Tata, M. Rajalakshmi, and A. K. Arora, *Phys. Rev. Lett.* **69**, 3778 (1992); T. Palberg and M. Würth, *ibid.* **72**, 786 (1994); B. V. R. Tata and A. K. Arora, *ibid.* **72**, 787 (1994).
- ²⁹C. P. Royall, M. E. Leunissen, and A. van Blaaderen, *J. Phys.: Condens. Matter* **15**, S3581 (2003); K. Ito, H. Yoshida, and N. Ise, *Science* **263**, 66 (1994).